

Session 1P6b

Guided Waves

| | |
|--|-----|
| Guide-Wave Propagation on 2D Doubly-Periodic Clusters of Multi-Port Resonators | |
| <i>R. A. Speciale (Research and Development Inc., USA);</i> | 416 |
| Dispersion Characteristics of Coplanar Waveguides at Subterahertz Frequencies | |
| <i>J. Zhang (University of Rochester, USA); T. Y. Hsiang (University of Rochester, USA);</i> | 417 |
| A Multi Conductor Transmission Line Model for the Evaluation of the Rotor Shaft Voltages in Adjustable Speed Drive Motors | |
| <i>B. de Vivo (University of Salerno, Italy); C. Petrarca (University of Naples, Italy); V. Tucci (University of Salerno, Italy); M. Vitelli (Second University of Naples, Italy);</i> | 421 |
| Frequency-selective Power Transducers “Hexagonal Ferrite Resonator—Semiconductor Element” | |
| <i>M. Y. Koledintseva (University of Missouri-Rolla, USA);</i> | 426 |
| Analysis of Guided Modes in Shielded Slot Line | |
| <i>F. Kuroki (Kure National College of Technology, Japan); K. Miyamoto (Kure National College of Technology, Japan);</i> | 431 |
| Propagation of Light in Random Waveguide Systems with Slightly Random Imperfections | |
| <i>A. Komiyama (Osaka Electro-Communication University, Japan);</i> | 432 |

Guide-Wave Propagation on 2D Doubly-Periodic Clusters of Multi-Port Resonators

R. A. Speciale

Research and Development Inc., USA

The recently introduced Tilted-Ellipse Representation of Standing-Wave Patterns [1,2] provides a fast and inexpensive way for extracting the multi-dimensional, complex scattering-matrices of very large, multi-port microwave systems, by performing computer-simulations of large-scale experimental-measurements that would require a very complex and expensive multi-port Automated Vector Network Analyzer, and a long data-acquisition time. That simulation method is based on the results of a rigorous mathematical analysis [1,2] of the simultaneous propagation of forward- and backward-waves along virtual measurement lines, connected to the ports of the microwave systems being simulated. That measurement-simulation method is currently being applied to the study of guided-wave propagation on 2D doubly-periodic clusters of directly-coupled, multi-port cylindrical resonators. Very large reductions of the problem-dimensionality is attained, by combining diakoptiks and symmetry-analysis. The complex scattering-matrix of C_{6V} -symmetric unit-cells is circulant, and symmetric around its main-diagonal, due to reciprocity, so that it may be specified using only the first three elements of its first row. Similar order-of-magnitude dimensionality-reductions are attained by interconnecting unit-cells in progressively-larger clusters having the same C_{6V} , and diagonal symmetry. The smallest cluster including only seven cylindrical-resonators is shown in Figure 1.

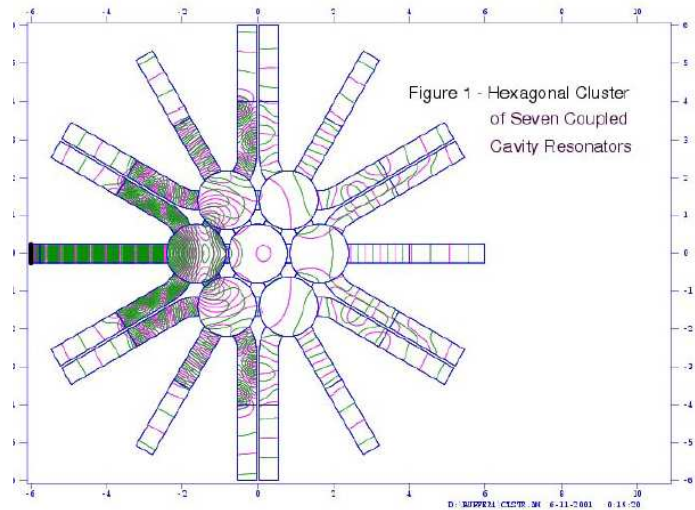


Figure 1:

Guided-wave propagation on such clusters of directly-coupled resonators is being characterized around the resonant frequencies of the TM_{010} and TM_{110} modes, including excitations generating left-/right-hand circular polarizations.

REFERENCES

1. Speciale, R. A., "Computing the scattering matrix of multiport systems," *PIERS 2004*, Pisa, Italy, 2004.
2. Speciale, R. A., "The tilted-ellipse representation of standing-wave patterns," *ACES 2004*, Syracuse, NY, 2004.

Dispersion Characteristics of Coplanar Waveguides at Subterahertz Frequencies

J. Zhang and T. Y. Hsiang
University of Rochester, USA

Abstract—We present experimental and simulated studies of the dispersion characteristics of coplanar waveguides (CPWs) at subterahertz frequencies. Two types of CPWs were studied, those with wide ground planes and those with narrow ground planes. In both cases, simulations closely followed the experimental results, thus giving us a basis for implementing the simulations in circuit-design models for a wide range of such waveguides.

1. Introduction

Coplanar waveguide (CPW) structures are commonly used in high-speed circuits and interconnect. Although the wave-propagation characteristics of CPWs have been well studied [1–11], only recently has this work been extended to the terahertz range for different geometries [6–9] and compared with experimental results [10, 11]. While our previous work focused on the attenuation characteristics [10, 11], in this paper we report results on the dispersion characteristics to complete the study. Our work is based on comparing experimental data with simulations that make use of full-wave analysis, allowing for direct verification of the validity of the latter. The effects of ground-plane width and lateral line dimensions have also been analyzed.

2. Background

CPWs are a family of transmission lines consisting of a center conductor strip and two ground conductor planes with variable widths. All three conductors are placed on the same side of a dielectric substrate, as shown in Figure 1.

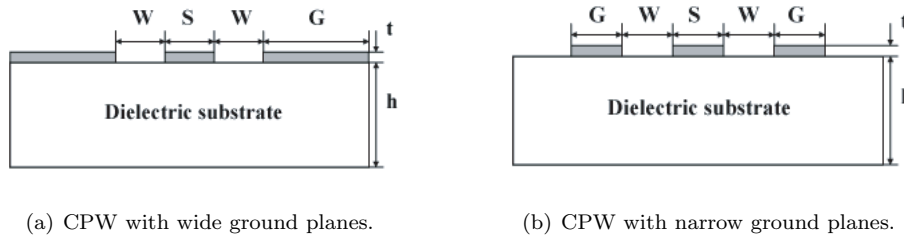


Figure 1: Cross-section of CPWs being investigated.

Two classes of CPWs were studied. The first contains ground planes at least 10 times wider than the center conductor or the conductor spacing and closely approximates an ideal CPW structure with infinitely wide ground planes. It should be pointed out that, for this class of transmission lines, closed-form analysis is in principle possible with the use of conformal mapping [12]. The second class uses ground planes with the same width as that of the center conductor, representing a practical geometry used in integrated circuits. For the latter category, theoretical studies are restricted to numerical simulations.

When an electromagnetic wave propagates on a CPW, the electric fields above conductors experience the permittivity of the air, while those below conductors experience the permittivity of the substrate. The effective permittivity thus takes on a value between that of the air and substrate. When the frequency of propagating wave increases, the effective permittivity approaches that of the substrate, as the density of electric field lines below the

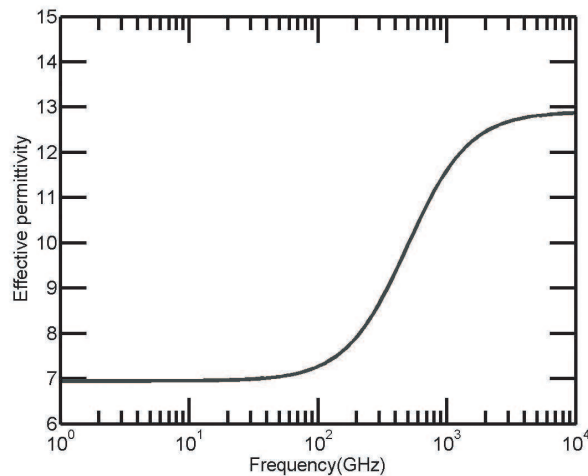


Figure 2: Effective permittivity of a CPW with wide ground planes. See Section 3 for geometry and electrical parameters.

conductors gets higher. The difference in the effective permittivity at different frequencies results in a modal dispersion that can be described with a frequency-dependent propagation constant:

$$\beta = 2\pi f \cdot 10^9 \cdot \frac{\sqrt{\varepsilon_{eff}}}{c} \quad (1)$$

where f is the frequency, c is the speed of light in free space, and ε_{eff} is the frequency-dependent effective permittivity. An example of ε_{eff} is demonstrated in Figure 2 [1].

Figure 2 shows that, with increasing frequency, the effective permittivity increases and a steep step is located at the position where the lowest-order surface-wave mode starts to interact with the CPW mode. For CPWs with infinitely wide ground planes, the TM_0 mode enters first and, at higher frequencies, this mode and higher-order modes contribute to the increase of ε_{eff} . For the case of narrow ground planes, the lowest-order surface-wave mode that can be supported is TE_0 mode [6]. Since the entry frequency of TM_0 mode is lower than that of TE_0 mode, CPW with wide ground planes supports more surface-wave modes and therefore suffers higher dispersion than CPW with narrow ground planes in the 100's GHz range.

3. Experiment and Simulation

In our work, the CPWs were fabricated on 500- μm -thick semi-insulating GaAs substrates. Gold was evaporated on the substrate and formed the transmission line patterns using a "lift-off" process [13]. The thickness of gold conductor was measured as $t = 290 \text{ nm}$. Each set of CPW had a center conductor and conductor spacing with a width of $S = W = 50$ or $10 \mu\text{m}$. The ground plane was chosen as $G = 500 \mu\text{m}$ for CPW with wide ground planes or as the lateral line dimension for CPW with narrow ground planes. With a testing method utilizing the non-uniform illumination of photoconductive switches together with electro-optic sampling, the broadband description of CPW characteristics has been obtained [11, 13]. The signal propagating along the CPW was measured in the time domain and then converted to the frequency domain by Fourier transform [13].

For comparison with the experiments, we used the software package Sonnet Suites to simulate the transmission lines. The simulation makes use of a modified method of moments based on Maxwell's equations to perform a three dimensional full-wave analysis of predominantly planar structures [14] and returns the values of the scattering matrices. The geometry and electrical parameters used for simulation are the same as those in the experiments. The simulated scattering matrices are then converted to propagation constant and, in turn, to the effective permittivity by (1).

4. Results and Discussion

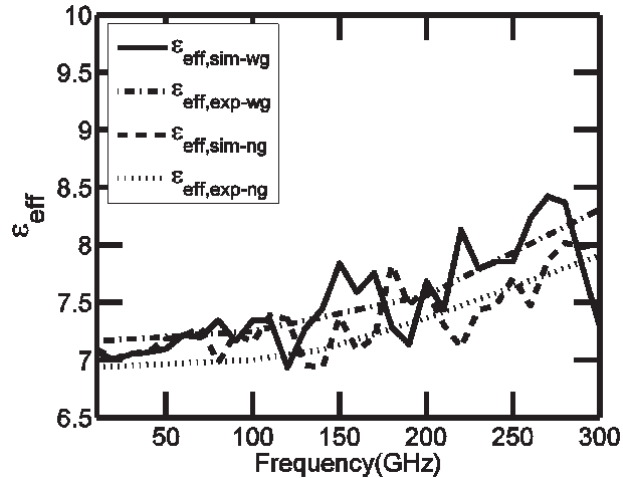


Figure 3: Simulated and experimental effective permittivity of CPWs with a 50- μm center conductor. $\varepsilon_{eff,sim-wg}$ and $\varepsilon_{eff,exp-wg}$ refer to simulated and experimental effective permittivity of the wide-ground CPW, respectively. $\varepsilon_{eff,sim-ng}$ and $\varepsilon_{eff,exp-ng}$ refer to simulated and experimental effective permittivity of the narrow-ground CPW, respectively.

Figure 3 shows the subterahertz effective permittivity of CPWs with a 50- μm center conductor as a function of the frequency. We present the simulated and experimental effective permittivity of CPWs with both wide and narrow ground planes for comparison. There is a good agreement except for the several peaks on the simulated

curves. These peaks are remnants of the poles in the Green's function used in the Sonnet Suites and correspond to the sequential entry of the surface-wave modes. Although the poles are removed one by one in the final results, some oscillations remain and are an unavoidable artifact.

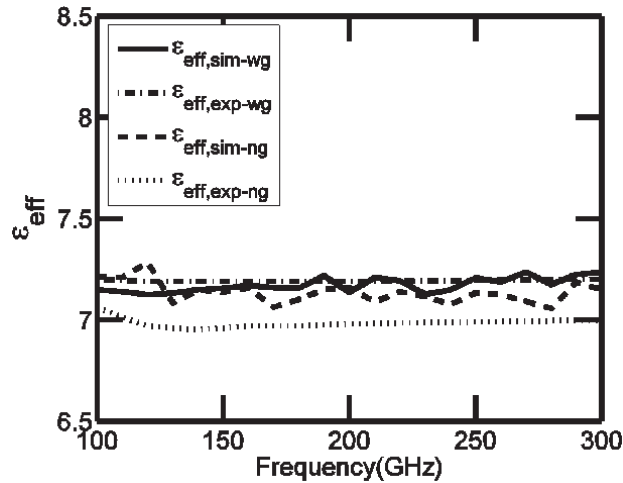


Figure 4: Simulated and experimental effective permittivity of CPWs with a 10- μm center conductor. $\epsilon_{eff,sim-wg}$ and $\epsilon_{eff,exp-wg}$ refer to simulated and experimental effective permittivity of the wide-ground CPW, respectively. $\epsilon_{eff,sim-ng}$ and $\epsilon_{eff,exp-ng}$ refer to simulated and experimental effective permittivity of the narrow-ground CPW, respectively.

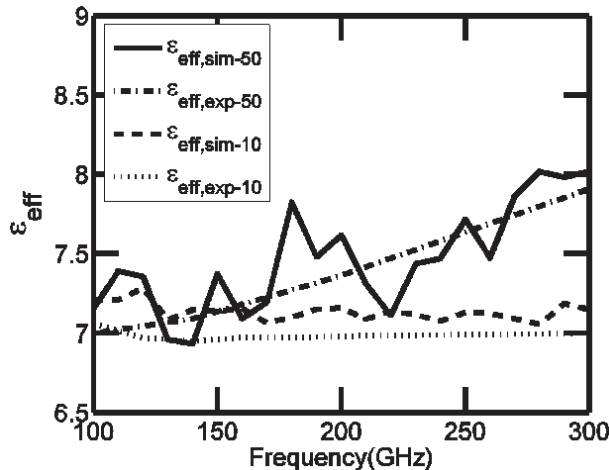


Figure 5: Simulated and experimental effective permittivity of CPWs with narrow ground planes. The lateral line dimensions are 50 μm and 10 μm , respectively. $\epsilon_{eff,sim-50}$ and $\epsilon_{eff,exp-50}$ refer to simulated and experimental effective permittivity of the CPW with a 50- μm center conductor, respectively. $\epsilon_{eff,sim-10}$ and $\epsilon_{eff,exp-10}$ refer to simulated and experimental effective permittivity of the CPW with a 10- μm center conductor, respectively.

An important observation of Figure 3 is that one clearly sees that the CPW with narrower ground planes returns a lower effective permittivity and reduced dispersion in both the experimental and simulated data. The reduced ground-plane width gives rise to a reduction in coupling between the CPW mode and surface-wave modes, which consequently decreases dispersion along the CPW.

We also investigated dispersion characteristics of CPWs with narrower lines. Figure 4 shows the subterahertz effective permittivity of CPWs with a 10- μm center conductor. Again, it can be seen that CPW with narrow ground planes encounters lower effective permittivity than CPW with wide ground planes. Dispersion is slightly improved in CPW with narrow ground planes.

To examine the effect of lateral line dimension, we combine the narrow-ground CPW data into Figure 5. It

is clearly seen that the effective permittivity of CPW with a 10- μm center conductor is lower than that of CPW with a 50- μm center conductor and the overall dispersion is much less.

5. Conclusion

In summary, we present experimental and simulated dispersion characteristics of CPWs with wide and narrow ground planes. The simulation results agree well with the experimental data up to subterahertz frequencies. It is shown that CPW with narrow ground planes suffers lower dispersion than CPW with wide ground planes. Furthermore, dispersion can be reduced by reducing the lateral line dimension of the CPW. Combining our previous studies on the attenuation characteristics [10, 11] and the current work on dispersion, we conclude that in the frequency range where radiation effects dominate (100's GHz for the lines considered in this report), the narrow-ground CPWs perform better in both aspects.

Acknowledgment

The authors wish to acknowledge the assistance of and discussion with Mr. B. Mu, the Rochester Institute of Technology, Rochester, NY, Professor H. Wu and Mr. Y. Zhu, the University of Rochester, Rochester, NY.

REFERENCES

1. Hasnain, G., A. Dienes, and J. R. Whinnery, "Dispersion of picosecond pulses in coplanar transmission lines," *IEEE Trans. Microwave Theory Tech.*, Vol. 34, No. 6, 738–741, 1986.
2. Jackson, R. W., "Considerations in the use of coplanar waveguide for millimeter-wave integrated circuits," *IEEE Trans. Microwave Theory Tech.*, Vol. 34, No. 12, 1450–1456, 1986.
3. Riazat, M., R. Majidi-Ahy, and I.-J. Feng, "Propagation modes and dispersion characteristics of coplanar waveguides," *IEEE Trans. Microwave Theory Tech.*, Vol. 38, No. 3, 245–251, 1990.
4. Phatak, D. S., N. K. Das, and A. P. Defonzo, "Dispersion characteristics of optically excited coplanar striplines: comprehensive full-wave analysis," *IEEE Trans. Microwave Theory Tech.*, Vol. 38, No. 11, 1719–1730, 1990.
5. Frankel, M. Y., S. Gupta, J. A. Valdmanis, and G. A. Mourou, "Terahertz attenuation and dispersion characteristics of coplanar transmission lines," *IEEE Trans. Microwave Theory Tech.*, Vol. 39, No. 6, 910–915, 1991.
6. Tsuji, M., H. Shigesawa, and A. A. Oliner, "New interesting leakage behavior on coplanar waveguides of finite and infinite widths," *IEEE Trans. Microwave Theory Tech.*, Vol. 39, No. 12, 2130–2136, 1991.
7. Ke, J. Y. and C. H. Chen, "Dispersion and attenuation characteristics of coplanar waveguides with finite metallization thickness and conductivity," *IEEE Trans. Microwave Theory Tech.*, Vol. 43, No. 5, 1128–1135, 1995.
8. Rastogi, A. K. and S. Hardikar, "Characteristics of CPW with thick metal coating," *Conference Digest, International Conference on Infrared and Millimeter Waves*, 345–346, 2002.
9. Schnieder, F., T. Tischler, and W. Heinrich, "Modeling dispersion and radiation characteristics of conductor-backed CPW with finite ground width," *IEEE Trans. Microwave Theory Tech.*, Vol. 51, No. 1, 137–143, 2003.
10. Zhang, J. and T. Y. Hsiang, "Subterahertz attenuation in coplanar waveguides," *Microwave Symposium Digest, 2005 IEEE MTT-S International*, 1905–1908, 2005.
11. Zhang, J., S. Alexandrou, and T. Y. Hsiang, "Attenuation characteristics of coplanar waveguides at subterahertz frequencies," *IEEE Trans. Microwave Theory Tech.*, Vol. 53, No. 11, 3281–3287, 2005.
12. Gupta, K. C., R. Garg, and I. J. Bahl, *Microstrip Lines and Slotlines*, Artech House, Norwood, MA, 1979.
13. Hsiang, T. Y., S. Alexandrou, and C. C. Wang, "Terahertz dispersion of coplanar waveguides and waveguide bends," *Proceedings of PIERS'95 — Progress in Electromagnetics Research Symposium*, 789, 1995.
14. *Sonnet User's Guide Release 10*, Sonnet Software Inc. Syracuse, NY, 2005.

A Multi Conductor Transmission Line Model for the Evaluation of the Rotor Shaft Voltages in Adjustable Speed Drive Motors

B. de Vivo¹, C. Petrarca², V. Tucci¹, and M. Vitelli³

¹University of Salerno, Italy

²University of Naples, Italy

³Second University of Naples, Italy

Abstract—The use of switching devices, such as IGBTs, characterised by high switching frequencies and very low switching times in new generation pulse width modulation (PWM) inverters has increased the efficiency and performances of Adjustable Speed Drives (ASDs) for industrial and traction applications. However, such systems may be affected by disadvantages like over voltages at the motor terminals, when long cables are used between the drive, and the generation of rotor shaft voltage, due to the capacitive couplings in the motor (between the windings and the rotor and between the rotor and the stator). The shaft voltage may cause the breakdown of the lubricating film in the bearings. The resulting impulsive currents, by damaging the bearing elements shorten the component life, which in turn seriously affects the ASD reliability. For this reason, it is of great importance to develop numerical models able to predict the shaft voltage so as to estimate the currents flowing through the bearings. Several works, based on either concentrated or distributed circuit models, have been proposed for the evaluation of the shaft voltage magnitudes for several motors sizes. However, the results obtained by such approaches suffer from approximations and simplifications in the considered circuit model. Therefore, in the present paper, a numerical model able to accurately predict the shaft voltage in high power induction motor for traction applications fed by a PWM inverter is presented. The windings of the motor are modelled by a multi conductor transmission line (MTL), whereas the cables between the source and the motor are described by a single transmission line. The effect of wave propagation and reflection and of the frequency-dependent distributed losses is considered by using a time-domain equivalent circuit to represent the MTL. A semi-analytical method, based on the perturbation theory of the spectrum of symmetric matrices, is adopted. The parameters of the MTL are obtained either analytically or numerically by using a commercial software (Maxwell® by Ansoft). The effects of the rise time of the input voltage together with the length of the cables are considered.

1. Introduction

A drive system composed of a traditional induction motor matched to a pulse-width modulated (PWM) inverter can overcome the limitations of induction motors operating directly on line voltage, consisting essentially in a nearly constant, unadjustable output speed and in a small starting torque, drawing a large starting current. By feeding the motor with a variable ac voltage and a variable ac frequency, thus obtaining an adjustable-speed drive (ASD), most requirements of modern drives can be satisfied. More recently, such systems have reached a great diffusion, which can be mostly associated to the rapid development of new switching devices, such as the insulated gate bipolar transistor (IGBT), which have led to increased efficiency, performance and controllability in medium voltage, medium power induction motor applications, such as traction, cranes for port operation, etc.

Unfortunately, the output voltage from the inverter is not purely sinusoidal and, in particular, steep front pulses can be generated in correspondence to the commutations of the switching devices. Slew rates (dV/dt) of about $2500\text{ V}/\mu\text{s}$ can be produced, resulting in overvoltages at the motor terminals and in critical stresses of the motor electrical insulation which can lead to a sensible reduction of the life-time of the machine [1].

Furthermore, it should be considered that such pulses can excite the capacitive coupling between the stator and the rotor, resulting in shaft voltages, even 20 times larger than those observed when feeding the motor with a pure sinusoidal waveform. The shaft voltages may cause the breakdown of the lubricating film in the bearings. The resulting impulsive currents, by damaging the bearing elements can shorten the component life, which in turn seriously affects the ASD reliability.

For design purposes, it seems, therefore, of great importance to provide the electrical engineers with a model able to predict the voltage distribution in the motor windings and evaluate the electrical stresses on the rotor shafts as a function of many geometrical and electrical parameters, such as the stator insulation dimension, the length of feeding cable, shape of the applied voltage, insulating material permittivity etc.

The model developed by Melfi et al., [2] is based on a representation of the motor winding as a lumped network; in order to preserve its physically distributed nature, the parasitic coupling between the stator and the rotor has been modelled over a range of frequencies. Also Lipo et al., [3] have used an equivalent lumped parameter π -network to describe the parasitic coupling phenomenon. They remark that the parasitic coupling circuits are the same as transmission line circuits, but a distributed parameter circuit is not suitable for a simplified analysis of the bearing currents.

The present paper is dedicated to the illustration of a machine model based on the representation of the motor winding as a connection of multiconductor transmission lines. The model is able to predict the voltages across the rotor shaft, taking into account the main phenomena occurring along the lines, such as the propagation and the reflection, together with the time dispersion introduced by the losses, eventually dependent on the frequency. The solution technique is accurately described in many papers [4]; it consists of a semi-analytical method based on the perturbation theory of the spectrum of symmetric matrices. The MTL lines are described by their characteristic \mathbf{R} , \mathbf{L} , \mathbf{C} , and \mathbf{G} per unit length matrices, that is, in the Laplace domain by the longitudinal impedance $\mathbf{Z}(s) = \mathbf{R} + s\mathbf{L}$ and transverse admittance $\mathbf{Y}(s) = \mathbf{G} + s\mathbf{C}$.

The authors explicitly remark that the paper is dedicated to the illustration of the model and its potentiality but, at present, not to the estimation of the shaft voltages in the motor operating conditions. In fact, as discussed in the following sections, the results of the simulations have been obtained by feeding the machine not with a typical three-phase inverter output voltage, but providing a single-phase ramp voltage with variable slew rate. It is the author's opinion that the findings are still extremely significant since they can describe the effects of slew rate (dV/dt) of the input voltage together with the length of the feeding cable adopted. Simulations in real operating conditions, together with experimental verifications will be the subject of future works.

In the following, section 2 is dedicated to an illustration of the basic model, together with a brief description of the solution technique; in section 3 the results of the numerical simulations are illustrated; the last section contains remarks, comments and proposals for the future activity.

2. The Model

A schematic representation of the model is reported in Fig. 1. An ideal ramp voltage generator is connected through a feeder cable to the motor. The stator winding is represented by a form wound stator coil, composed of conductors of rectangular cross section; it faces the rotor iron laminations; the rotor is connected to a pair of bearings represented in the picture by their equivalent capacitance C_{b1} and C_{b2} .

The system can be studied (Fig. 2) as single transmission line, representing the cable, connected to four multiconductor transmission lines in series placed in the slot and overhang regions of the machine. Further details can be found in [5] by Lupò et al., The MTL are composed of n conductors; the n -th conductor represents the rotor iron.

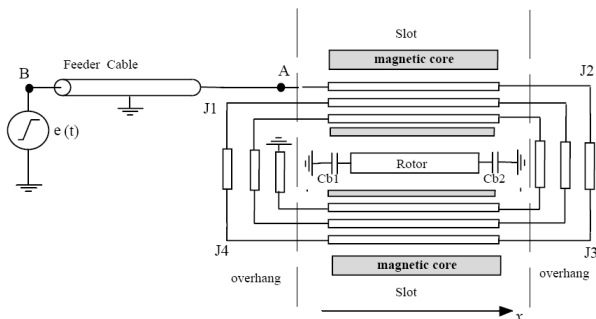


Figure 1: Schematic representation a motor phase.

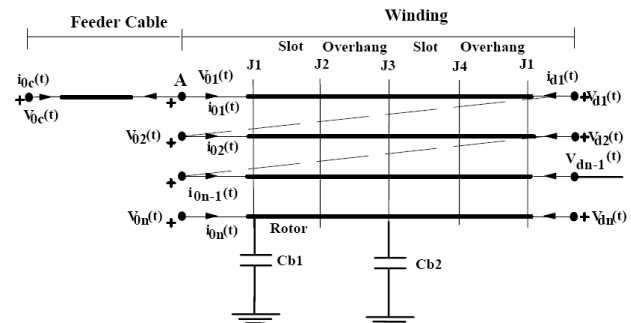


Figure 2: MTL model of the machine.

The multiconductor line can be studied in the time-domain by means of a $2n$ -ports representation (Fig. 3) described by Eqs. (1) and (2) [4]:

$$\begin{cases} \mathbf{i}_0(t) = \int_{0^-}^{t^+} \mathbf{Y}_c(t-\tau)\mathbf{v}_0(\tau)d\tau + \mathbf{j}_0(t) \\ \mathbf{i}_d(t) = \int_{0^-}^{t^+} \mathbf{Y}_c(t-\tau)\mathbf{v}_d(\tau)d\tau + \mathbf{j}_d(t) \end{cases} \quad (1)$$

$$\begin{cases} \mathbf{j}_0(t) = \int_{0^-}^{t^+} \mathbf{P}(t-\tau)[-2\mathbf{i}_d(\tau) + \mathbf{j}_d(\tau)]d\tau \\ \mathbf{j}_d(t) = \int_{0^-}^{t^+} \mathbf{P}(t-\tau)[-2\mathbf{i}_0(\tau) + \mathbf{j}_0(\tau)]d\tau \end{cases} \quad (2)$$

The impulse responses $\mathbf{Y}_c(t)$ and $\mathbf{P}(t)$ are defined as:

$$\begin{cases} \mathbf{Y}_c(t) = \mathbf{L}^{-1}[\mathbf{Y}_c(s)] = \mathbf{L}^{-1} \left[\sqrt{\mathbf{Z}^{-1}(s)\mathbf{Y}^{-1}(s)\mathbf{Y}(s)} \right] \\ \mathbf{P}(t) = \mathbf{L}^{-1}[\mathbf{P}(s)] = \mathbf{L}^{-1} \left[\exp \left[-d\sqrt{\mathbf{Y}(s)\mathbf{Z}(s)} \right] \right] \end{cases} \quad (3)$$

where $\mathbf{Y}_c(s)$ is the characteristic admittance and $\mathbf{P}(s)$ is the propagation function.

$\mathbf{Y}_c(t)$ and $\mathbf{P}(t)$ can be found as a sum of their principal part, i.e., the parts containing terms as Dirac pulses, and a remainder evaluated by performing a numerical inverse transform. The solution can be achieved by means of a recursive approach since at time instant t the state variables $\mathbf{j}_0(t)$ and $\mathbf{j}_d(t)$ are known because they depend on the values assumed at time instant $(t - T)$ by themselves and by the currents, where T is the propagation time delay.

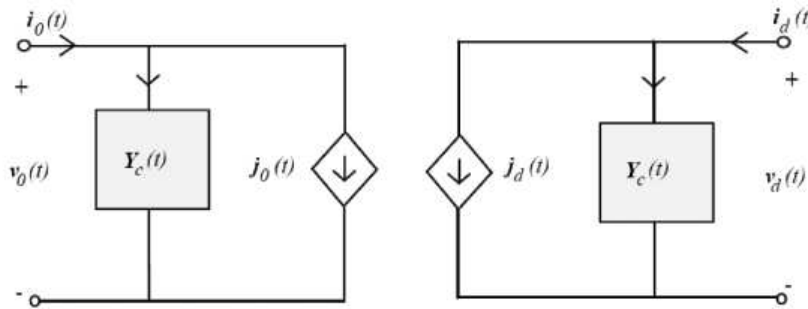


Figure 3: 2n-ports representation of a MTL.

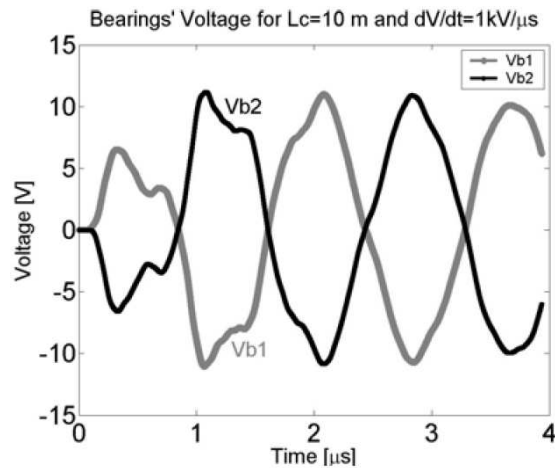


Figure 4: Bearings' voltages $V_{b1}(t)$ and $V_{b2}(t)$.

3. Results of Numerical Simulation

The numerical simulations have been carried out on a traction motor characterised by 9 conductors per slot. The applied voltage has a maximum value $E_{max} = 750 \text{ V}$ and a variable slew rate chosen in the interval $(0.5 \div 2.0 \text{ kV}/\mu\text{s})$; the length L_c of the feeder cable varies between 5 m and 15 m. The equivalent capacitances C_{b1} and C_{b2} are chosen equal to 5 nF. Prior to the numerical simulation the p.u. length matrices, \mathbf{C} and \mathbf{L} have been evaluated with the software packing Maxwell® by solving, respectively, an electrostatic and a magnetostatic problem.

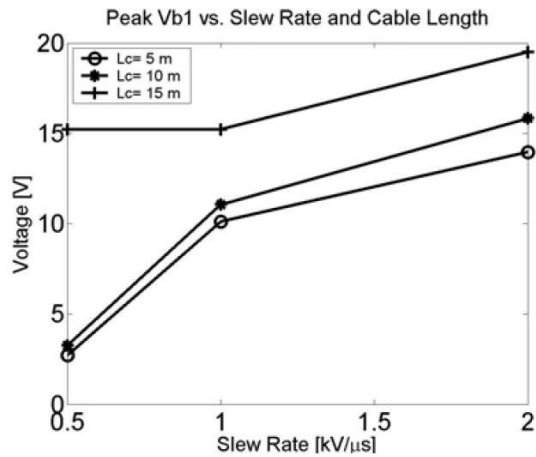


Figure 5: Peak value of V_{b1} vs dV/dt and L_c .

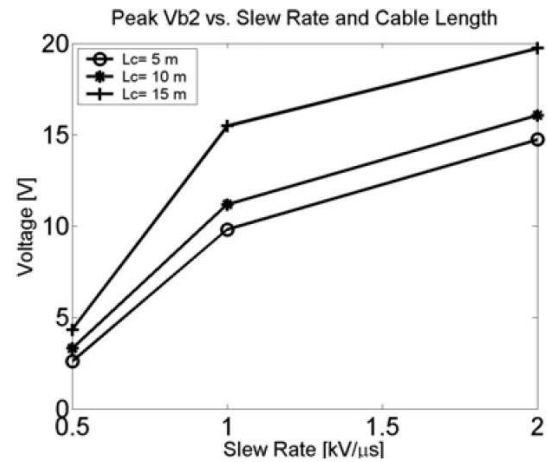


Figure 6: Peak value of V_{b2} vs dV/dt and L_c .

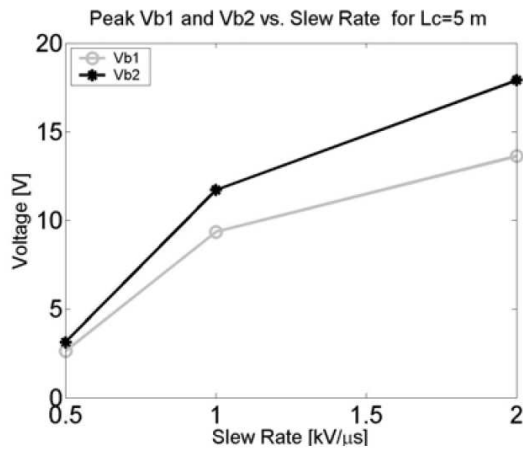


Figure 7: Peak value of V_{b1} and V_{b2} vs. dV/dt .

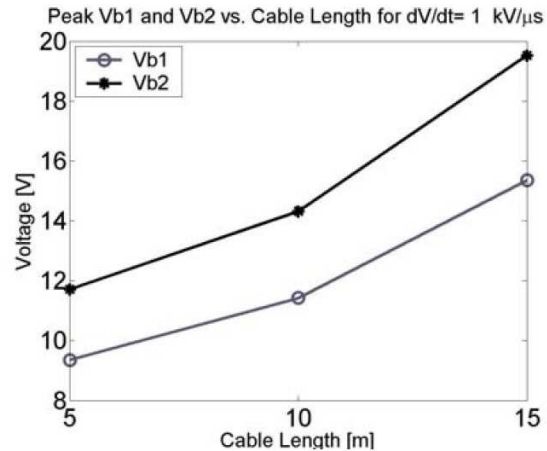


Figure 8: Peak value of V_{b1} and V_{b2} vs. L_c .

As an example of the results obtained, in Fig. 4 the time evolutions of the voltage $V_{b1}(t)$ and $V_{b2}(t)$ across the two bearings are reported when $dV/dt = 1 \text{ kV}/\mu\text{s}$ and $L_c = 10 \text{ m}$. Voltage $V_{b2}(t)$ is slightly delayed with respect to $V_{b1}(t)$, due to a propagation delay of about 40 ns.

Since the main parameter influencing the breakdown phenomena in the lubricating film in the bearings is the maximum amplitude V_m of the voltage, in Figs. 5 and 6 the peak values of V_{b1} and V_{b2} are reported as a function of the slew rate and the cable length.

In particular, it is evident that critical situations can be reached with long cables and high slew rates: the peak voltages can be almost 5 times higher with $L_c = 15 \text{ m} - dv/dt = 2.0 \text{ kV}/\mu\text{s}$ if compared with $L_c = 5 \text{ m}$ and $dv/dt = 0.5 \text{ kV}/\mu\text{s}$. Furthermore, the peak voltages can be different for the two bearings and, as a consequence, the breakdown phenomena can occur only in one bearing.

Such a difference is amplified when the bearings' capacitances are not equal, for instance when bearings of different type are installed (bearings produced by diverse manufacturers, standard or insulated bearings, new or aged bearings, etc.). In fact, when introducing in the simulations two values for such capacitances ($C_{b1} = 4 \text{ nF}$;

$C_{b2}=5\text{ nF}$), the difference in the peak values of V_{b1} and V_{b2} is strongly evident, as shown in Figs. 7 and 8. In particular, the dissimilarity between peaks of V_{b1} and V_{b2} grows with the slew rate and the length of the feeding cable.

4. Conclusions

The present paper describes an equivalent MTL model able to predict the shaft voltages in high power induction motor for traction applications fed by a PWM inverter. By feeding the motor with an ideal ramp voltage generator, it is possible to derive significant information on the voltages across the motor bearings; their peak values strongly depend on the slew rate of the applied voltage and on the length of the connecting cable. The effect of different bearings' capacitances has also been evidenced. Further work is in progress in order to introduce a typical three-phase inverter output voltage and to clarify the effect of other parameters like the amplitude of the applied voltage, the electrical characteristics of the cables, the geometrical parameters of the machine.

REFERENCES

1. Bonnett, A. H., "Analysis of the impact of pulse-width modulated inverter voltage waveforms on ac induction motors," *IEEE Trans. on Industry Applications*, Vol. 32, 386–392, 1996.
2. Naik, R., T. A. Nondhal, M. Melfi, R. Schiferl, and J. Wang, "Circuit model for shaft voltage prediction in induction motors fed by pwm-based ac drives," *IEEE Trans. on Industry Applications*, Vol. 39, No. 5, 1294–1299, 2003.
3. Chen, S., T. A. Lipo, and D. Fitzgerald, "Modelling of motor bearing currents in PWM inverter drives," *IEEE Trans. on Industry Applications*, Vol. 32, No. 6, 1365–1370, 1996.
4. Maffucci, A. and G. Miano, "Irregular terms in the impulse response of a multiconductor lossy transmission line," *IEEE Trans. on Circuit and Systems.*, Vol. 46, No. 7, 788–805, 1999.
5. Lupò, G., C. Petrarca, V. Tucci, and M. Vitelli, "Multiconductor transmission line analysis of steep-front surges in machine windings," *IEEE Trans. on Dielectrics and Electrical Insulation*, Vol. 9, No. 3, 467–478, 2002.

Frequency-selective Power Transducers “Hexagonal Ferrite Resonator—Semiconductor Element”

M. Y. Koledintseva
University of Missouri-Rolla, USA

Abstract—The transducers studied herein allow for frequency-selective measurement of mm-wave power parameters. Frequency selectivity is assured by a monocrystalline hexagonal ferrite resonator (HFR). The HFR is in direct contact with a semiconductor element (SE)—an unpackaged Hall-element, or a chip transistor (or diode). Power absorbed by the HFR at the ferromagnetic resonance converts to heat, and the heat flux penetrates through the current-carrying SE. A number of thermo/electro/magnetic phenomena accompany the Hall-effect in a semiconductor and cause a voltage in addition to the Hall-effect voltage. The conversion coefficient of a transducer is analyzed using the power balance equation. Some experimental results using the designed power transducers in the 8-mm waveband are presented.

1. Introduction

Many applications require an adequate information about mm-wave (30–300 GHz) spectra of signals, e.g., spectral power density, peak power of pulse signals, integral power in the given frequency band, width and central frequency of spectrum [1, 2]. Equipment for measuring power parameters of electromagnetic signals contains a primary measuring transducer and a secondary processing/display unit. A primary transducer in this case converts the energy associated with electromagnetic oscillations into a different form of energy (e.g., thermal, mechanical, etc.), or into voltage which is convenient to register and quantify. Most of microwave and mm-wave power meters and detectors are not frequency-selective. Their application for “fine” spectra measurements needs additional high-Q filters and cumbersome calibration of the receiving path. Heterodyne-type spectrum analyzers and measuring receivers typically have numerous parasitic channels of reception, which is an especially difficult problem for the analysis of mm-wave spectra of signals of middle and higher intensity levels (more than 1 mW of continuous power).

The transducers proposed herein allow for frequency-selective measuring of mm-wave power parameters. Frequency selectivity is assured by incorporating a monocrystalline hexagonal ferrite resonator (HFR) with a narrow ferromagnetic resonance (FMR) line. An advantage of an HFR is its high intrinsic field of magnetic crystallographic anisotropy, so it does not need massive bias magnetic systems for achieving FMR [2]. In the transducer, the HFR is in direct contact with a semiconductor element (SE). The SE may be an unpackaged Hall-element (HE) slab, or chip transistor (or diode). The mm-wave power absorbed by the HFR at the FMR converts to heat, and the heat flux from the HFR penetrates through the body of the current-carrying SE. Since this structure is in the bias magnetic field, there are a number of thermoelectric, thermomagnetic, galvanomagnetic, and thermoelectromagnetic phenomena, along with the Hall-effect in the SE. In fact, there are over 560 different known effects accompanying the Hall-effect [3]. These phenomena cause a voltage in addition to that of the Hall-effect. This happens only when the frequency of the mm-wave signal falls into the ferromagnetic resonance curve of the HFR, thereby assuring frequency selectivity of power conversion.

2. Mathematical Model for the Conversion Coefficient of the Transducer

The conversion coefficient of a frequency-selective power transducer is defined as a ratio of the amplitude of the converted signal to the power of the input microwave signal at the given frequency [1],

$$K_p = \Delta V / P(f_0). \quad (1)$$

If the thermal coefficient of voltage in a semiconductor element

$$K_T = \Delta V / \Delta T \quad (2)$$

is known, then the conversion coefficient of a transducer operating on the basis of thermal effects is

$$K_p = K_T \Delta T_{stat} / P(f_0), \quad (3)$$

where ΔT_{stat} is the stationary temperature increase in the system “HFR-semiconductor element”.

Consider the case when a microwave oscillation of power $P(f_0)$ acts on the HFR continuously, and the HFR absorbs this power due to the FMR. Inside the HFR there is a constant source of heat, and the surface temperature of the HFR remains constant. Suppose that heat radiation is absent. Let us also neglect semiconductor

heating when current flows in it, and further assume there is no difference in the temperature of the contacts (no thermal electromotive force). The result of the semiconductor heating is the variation in the charge carrier mobility, which leads to the variation of the thermal coefficient K_T . Then the equation for thermal balance can be written in terms of power,

$$P_{abs} = P_{FS} + P_{SM} + P_{FA} + P_{SA}, \quad (4)$$

where $P_{abs} = \alpha P(f_0)$ is the mm-wave power absorbed by the ferrite at the FMR (α is the absorption coefficient); P_{FS} is the heat power transferred by the ferrite to the semiconductor element (conduction heat exchange); P_{SM} is the heat power transferred from the semiconductor element to the metal contacts (conduction heat exchange); P_{FA} is the heat power transferred by the HFR surface to air (convection heat exchange); and P_{SA} is the heat power given to air by the semiconductor (convection heat exchange).

The Cauchy problem describing the transient thermal regime in the system ‘‘HFR-SE’’ with a heat source inside the ferrite is analogous to that considered in [4] for a YIG bolometer,

$$C_\Sigma \frac{dT}{dt} + \Psi_{T\Sigma} T = P_{abs}; \quad T(0+) = T_r, \quad (5)$$

where C_Σ [J/K] is the total heat capacity of all the elements of the thermal system, and $\Psi_{T\Sigma}$ [W/K] is the total heattransfer factor of all the system. The initial condition is the room temperature T_r . The solution of the Eq. (5) is an exponential function

$$T(t) = T_r + \Delta T_{stat}(1 - e^{-t/\tau_\Sigma}), \quad (6)$$

where $\Delta T_{stat} = P_{abs}/\Psi_{T\Sigma}$ is the increase of the stationary temperature, and $\tau_\Sigma = C_\Sigma/\Psi_{T\Sigma}$ is the response time of the system.

The absorption coefficient α depends on the HFR rate of coupling with the transmission line where it is placed. This coupling is described by the coupling coefficient η_c [5], and in turn, it depends on the geometry of the transmission line or waveguide, operating mode structure, the point where the HFR is situated, and the physical parameters of the HFR (its resonance line width ΔH , saturation magnetization M_S , anisotropy field H_A , and orientation of the HFR crystallographic axis in respect with the bias magnetic field H_0), as well as on the detuning $|f_{res} - f_0|$ of the FMR frequency from the mm-wave signal carrier frequency. The absorption coefficient can be obtained through solving the self-matched field problem and electromagnetic power balance equation, as described in [1, 5]. From this analysis, the absorption coefficient relates to the coupling coefficient as

$$\alpha = 2|\eta_c|/|1 + \eta_c|. \quad (7)$$

For a transmission line or waveguide operating with only a single mode having transverse microwave magnetic field components $h_{x,y}$, and with the bias magnetic field for the HFR directed along z -direction, the coupling coefficient can be calculated as

$$\eta_c = j \frac{\omega \mu_0 V_f}{2N_1} (\chi_{11}^{ext} h_x^2 + \chi_{22}^{ext} h_y^2), \quad (8)$$

where $\chi_{11,22}^{ext}$ are the complex diagonal components of the external magnetic susceptibility tensor for an ellipsoidal (general case) HFR [1, 5] for any arbitrary orientation of the HFR crystallographic axis with respect to the bias magnetic field. In (8), V_f is the volume of the HFR, and N_1 is the norm of the corresponding transmission line or waveguide mode, as calculated in [5].

3. Calculations and Experimental Data

The calculations were performed for a uniaxial monocrystalline HFR resonator made of M-type Ba ferrite doped with Ti and Zn ions. It was placed in a metal waveguide with a cross-section of 7.2 mm \times 3.4 mm, in the point with the right circular polarization of the mm-wave magnetic field. The HFR in this case was a spheroid with the axes 0.585 mm \times 0.557 mm. Its magnetic parameters were the following: the field of crystallographic magnetic anisotropy was $H_A = 11.3$ kOe, saturation magnetization was $4\pi M_S = 3.5$ kG, and the unloaded resonance line width was $\Delta H = 31.1$ Oe. The density of the hexagonal ferrite was $\rho_f = 4900$ kg/m³; the specific heat was $c_f = 1100$ J/(kg.K); and thermal conductivity was $\lambda_f = 4.1$ W/(m.K). The measured input average power of the mm-wave continuous signal at the frequency $f_0 = 39.5$ GHz was $P(f_0) = 60$ mW; the HFR absorbed 5 dB at the FMR ($P_{abs}^{meas} = 41.1$ mW).

The Hall-element (HE) X511 (Russia) measured 1.5 mm \times 2.0 mm \times 0.1 mm. It was made of a monocrystalline InSb, the density was $\rho_s = 5770$ kg/m³, the specific heat was taken as $c_s = 700$ J/(kg.K); the thermal conductivity was $\lambda_s = 18$ W/(m.K); and the thermal coefficient of voltage K_T was 1.5 mV/K (according to the technical passport for the X511). An active region of contact with the HFR was assumed to be 0.01 mm². Heat transfer coefficients for natural convection (room temperature $T_r = 20^\circ C$ and normal atmosphere pressure of 760 mm of mercury) for both HFR and SE are about 30 W/(m².K).

The total heat transfer factor was calculated as $\Psi_{T\Sigma} = \Psi_{conv} + \Psi_{cond} = 1.2 \cdot 10^{-3} \text{ W/K}$. The total heat capacity is $C_{\Sigma} = C_f + C_s = 0.9 \cdot 10^{-3} \text{ J/K}$. The calculated response time of the system is $\tau_{\Sigma}^{calc} = 750 \text{ ms}$, and the calculated stationary temperature increase in the system is $\Delta T_{stat}^{calc} = 25^{\circ}\text{C}$. The transition time for the temperature increase is $t_{stat} = 4.6 \cdot \tau_{\Sigma} = 3.45 \text{ s}$. The calculated voltage at the SE is $\Delta V^{calc} = 37.5 \text{ mV}$, and the conversion coefficient is $K_p^{calc} = 0.625 \text{ V/W}$. The measured data are $\Delta T_{stat}^{meas} = 21^{\circ}\text{C}$ and $\tau_{\Sigma}^{meas} \approx 1 \text{ s}$.

4. Design and Experimental Data of the Frequency-selective Thermal Transducers

4.1. HFR-two Hall-elements

The structure of the frequency-selective electronically tunable power transducer is shown in Fig. 1. It contains two identical Hall elements: one is inside the waveguide, having direct contact with the HFR, and the second is on the outer side of the waveguide. Both transducers are exposed to the same uniform bias magnetic field. The Hall elements are connected so that it is possible to obtain a differential signal at the comparator. When there is no FMR absorption, the signals of the Hall elements are the same and correspond to the pure Hall-effect voltage in the given magnetic bias field. When the HFR is at the FMR, it heats up because of the resonance absorption, and there is an additional voltage that is induced on the contacts of the internal Hall element. Its value is proportional (with the coefficient K_P) to the average power of the mm-wave signal at the resonance frequency of the HFR, through the equation $\Delta V_H = K_P P_{av}(f_{res})$.

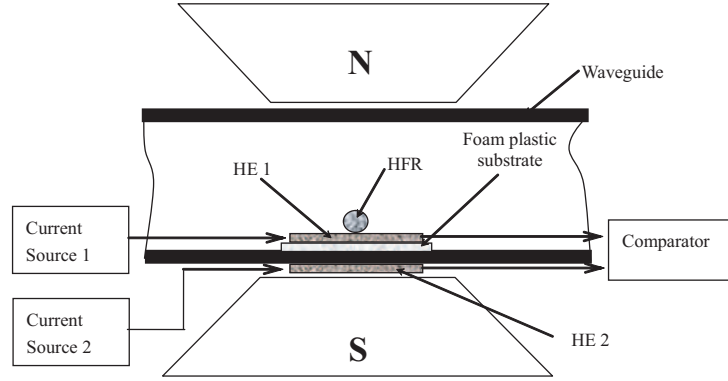


Figure 1: Schematic of the transducer based on the HFR and two Hall-elements.

When experimental structures based on the HFR and semiconductor elements were exposed to nanosecond pulses with pulse repetition frequency of 1 kHz, an off-duty factor of 2, and an average power of 10–100 mW, the mechanism of interaction was mainly inertial, of a thermal nature. Low-inertial effects, such as the magnetoresistive effect, the microwave Hall-effect in semiconductor, direct electromagnetic field detection by the SE, and magnetic detection by the SE due to variation in the magnetic flux from the HFR are negligibly small at average power levels of a few dozen mW. This inertial mechanism of interaction between the HFR and the mm-wave field is determined by heating of the HFR at the FMR power absorption and the corresponding heat flux acting on the Hall element.

Suppose that the total voltage induced in the semiconductor plate carrying a current I placed in a transverse magnetic field H_{0z} consists of a Hall-effect voltage V_H and a number of additional terms, corresponding to the most important effects accompanying the Hall-effect [3]:

$$V = V_H + V_{neq} + V_{mr} + V_{temf} + V_E + V_{NE} + V_{PNE} + V_{RL} + V_{PRL}. \quad (9)$$

In (9), V_{neq} is the non-equipotentiality voltage, V_{mr} is the magnetoresistive voltage, V_{temf} is the thermoelectromotive force voltage, V_E is the Ettingshausen galvanomagnetic voltage, V_{NE} is the Nernst- Ettingshausen thermomagnetic voltage, V_{PNE} is the Peltier-Nernst-Ettingshausen thermomagnetic electrothermal/ thermogalvanomagnetic voltage, V_{RL} is the Righi-Leduc thermomagnetic voltage, and V_{PRL} is the Peltier-Righi- Leduc electrothermal/thermogalvanomagnetic voltage. In the proposed design, the contribution of V_H and V_{mr} is compensated by the second Hall-element. The voltages V_{neqv} and V_{temf} are independent of the bias magnetic field, and can be taken into account and compensated. It is impossible to separate the remaining five contributions. However, the Nernst-Ettingshausen effect might be dominant. It is a thermomagnetic effect, and appears as a

transverse voltage with respect to the current I flowing in the semiconductor slab, assuming the latter is in the magnetic field and is affected by the heat flux.

In the experiment, two Hall elements were used. The first one was an X511 characterized by $R_{in} = 2.0$ Ohms, $R_{out} = 1.6$ Ohms, $I_{oper} = 100$ mA, and having a thermal sensitivity of 1.05 V/(A·T). The second was X211. The characteristics of the X211 differ only in the output resistance ($R_{out} = 1.9$ Ohms) and the thermal sensitivity 1.38 V/(A·T). The slope with respect to the magnetic field is $S = \Delta V / \Delta H = 10^{-2}$ mV/Oe for both Hall-elements. The minimum measured magnetic field for both Hall elements was 0.1 Oe. Identical operation of both Hall-elements was assured by proper choosing of their operation currents.

In the transducer, the first Hall-element was placed in the rectangular waveguide with cross-section 7.2 mm \times 3.4 mm, in the point of the circular polarization of the mm-wave magnetic field. The off-resonance loss factor in the section was 1.1 dB, and the standing wave ratio in this section was $SWR=1.2$. The HFR was the same as discussed above. The FMR absorption was 5 dB. Fig. 2 shows the resonance dependence of the differential signal ΔV as a function of the applied bias magnetic field H_{z0} for a continuous mm-wave signal at $f_0 = 40.7$ GHz. The minimum stable measured signal was about 10 μ W. The conversion coefficient was $K_P^{meas} = 0.6$ V/W, which is close to the calculated value ($K_P^{calc} = 0.625$ V/W). The discrepancy can be explained by the mm-wave loss in the section of the waveguide. The 50% alcohol solution of the glue BF-2 (Russia) was used to fix the HFR on the unpackaged HE, and the resonance absorption in a high-Q ferrite resonator could have decreased by about 1 dB due to the glue. The simplifying assumptions in the model, such as neglecting the heat loss on metal contacts, might also adversely influence the accuracy of computations. Also, the reference input data for the parameters of a transmission line, ferrite resonator, and InSb HE might have some tolerance. Furthermore, instrument error in the mm-wave measurements might yield another 1 dB of uncertainty.

4.2. HFR—Unpackaged Chip Diode or a Transistor

The Hall-element contacting with the HFR was replaced by a chip transistor (CT) used as a diode. The voltage thermal sensitivity of the CT (2TC398A-1 manufactured in Russia) was 3.0 mV/K, which is higher than the voltage thermal sensitivity of the HE. The HFR anisotropy field was $H_A = 10.6$ kOe, and the FMR line width was $\Delta H = 30$ Oe. The HFR absorbed 3 dB of power at the FMR ($f_0 = 40.7$ GHz, $P(f_0) = 60$ mW). The conversion coefficient is 1.2 V/W, which is two times greater than that of the transducer “HFR-2 Hall elements”. The minimum measured signal was about 1 μ W. The shortcoming of the transducer is the presence of a “pedestal” at the level of 1 mV due to the off-resonance heating of the semiconductor element directly from the mm-wave signal power. However, this “pedestal” can be removed by a calibration in the off-resonance regime. A further improvement of the transducer can be realized by using a more thermosensitive semiconductor element. Linear volt-watt characteristics of the transducers with two Hall-elements and the chip transistor are shown in Fig. 3.

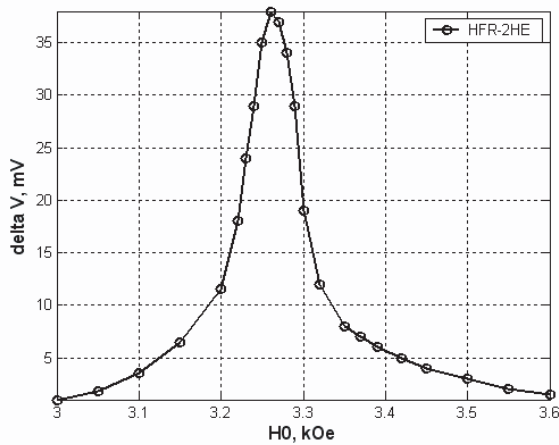


Figure 2: Resonance dependence of the converted voltage (HFR-2 Hall elements).

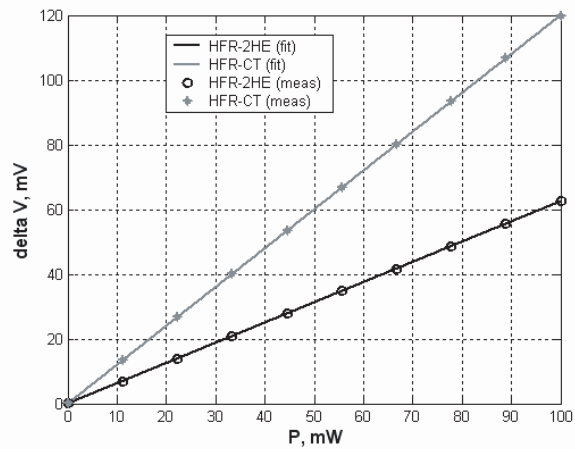


Figure 3: Linear volt-watt characteristics for transducers.

5. Conclusion

The transducers based on a high-Q hexagonal ferrite resonator in direct contact with a thermosensitive semiconductor element allow for frequency-selective measurement of mm-wave power parameters over a wide frequency range. The physical mechanisms of power conversion are analyzed, and it is shown that the conversion coefficient of a transducer can be calculated using the equation of power balance. To increase the sensitivity and conversion coefficients of a transducer based on the approach, it is necessary to use an HE with a higher thermal coefficient of voltage, assure the best possible heat contact between the HFR and the semiconductor element (increase the surface of their contact, for example, using a disk HRF), and employ a microvoltmeter with higher sensitivity to register smaller converted signals.

REFERENCES

1. Kitaytsev, A. A. and M. Y. Koledintseva, "Physical and technical bases of using ferromagnetic resonance in hexagonal ferrites for electromagnetic compatibility problems," *IEEE Trans. Electromag. Compat.*, Vol. 41, No. 1, 15–21, Feb. 1999.
2. Koledintseva, M. Y., A. A. Kitaitsev, V. A. Konkin, and V. F. Radchenko, "Spectrum visualization and measurement of power parameters of microwave wide-band noise," *IEEE Trans. Instrum. Measur.*, Vol. 53, No. 4, 1119–1124, Aug. 2004.
3. Kuchis, E. V., "Methods for investigation of the Hall-effect," Sov. Radio, Moscow, Russian, 1974.
4. Bogdanov, G. B., "Theory of inertial nonlinear phenomena in ferrites at microwaves," *Physical and Physico-Chemical Properties of Ferrites*, 297–309, Minsk, Russian, 1966.
5. Koledintseva, M. Y. and A. A. Kitaitsev, "Modulation of millimeter waves by acoustically controlled hexagonal ferrite resonator," *IEEE Trans. Magn.*, Vol. 41, 2368–2376, Aug. 2005.

Analysis of Guided Modes in Shielded Slot Line

F. Kuroki and K. Miyamoto
Kure National College of Technology, Japan

Guided modes in a shielded slot transmission line were analyzed. This transmission line consists of slotted metal strips inserted in a below cutoff parallel metal plate waveguide as shown in Fig. 1. The TEM mode as shown in Fig. 2(a) can propagate in the slot area as the lowest dominant mode, while the higher modes as shown in Fig. 2(b) may propagate in the metal strip regions. With this in mind, we calculated the cutoff wavelength based on the transverse resonant method. Figs. 3(a) and (b) show the quarter cross section and its transverse equivalent transmission-line circuit. From this equivalent circuit, the cutoff wavelength of the N th higher mode was given by

$$\lambda_c = \frac{1}{N - \frac{1}{\pi} \tan^{-1} \frac{B_s}{Y_0^{(1)}}} \left\{ w - s + \frac{\lambda_c}{\pi} \tan^{-1} \frac{B_a}{Y_0^{(1)}} \right\},$$

where B_a and B_s correspond to susceptances at the side edges of the metal strip, and $Y_0^{(1)}$ is the characteristic admittance of the TM mode propagating along the transverse equivalent transmission-line. The susceptances were calculated by the variational method for waveguide discontinuities. Fig. 4 shows the calculated and measured dispersion curves of the dominant TEM mode and the 1st higher mode. Agreement between the theory and measurement was quite satisfactory, and thus the validity of this analytical procedure was confirmed.

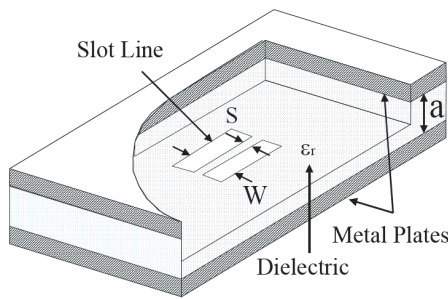


Figure 1: Structure of shielded slot line.

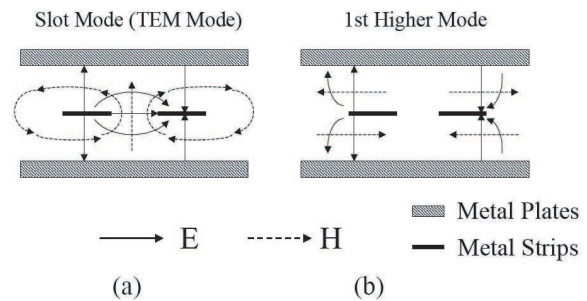


Figure 2: Field distributions of (a) slot mode and (b) 1st higher mode.

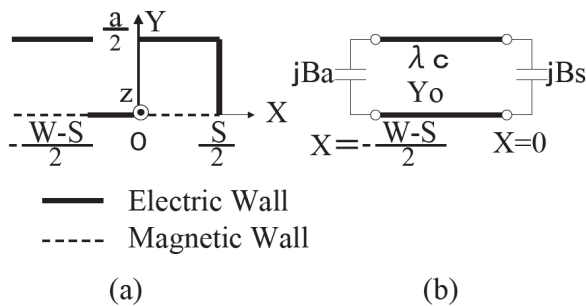


Figure 3: Analytical model. (a) Quarter cross sectional view, (b) Transverse equivalent transmission-line circuit.

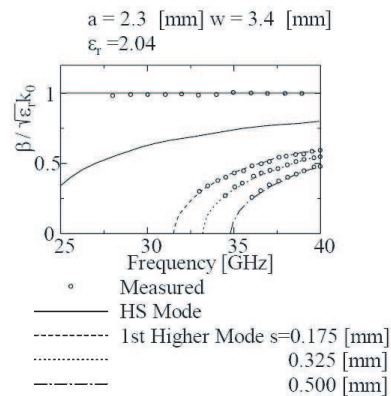


Figure 4: Calculated and measured dispersion curves of guided modes in shielded slot line.

Propagation of Light in Random Waveguide Systems with Slightly Random Imperfections

A. Komiyama

Osaka Electro-Communication University, Japan

From the interest in the crosstalk [1] in an image fiber which is used to transmit directly an optical image, the propagation properties of light in one-dimensional waveguide systems with random geometrical imperfections have been discussed based on the couple mode theory [2, 3]. In the numerical discussion [2] the propagation constants of the modes are generated by using a series of random normal numbers and the coupled mode equation is numerically solved. Although there is no essential difficulty, the numerical calculations for a large system with a very long correlation length are a time consuming task. Besides from the numerical results it is difficult to understand the whole of the dependence of the propagation properties on the structure parameters of the system. In the theoretical discussion [3] the perturbation solution of the couple mode equation is used. Consequently the results obtained are applicable only to the case of a short correlation length.

In this paper a propagation problem of light in a one-dimensional waveguide system composed of an infinite number of cores is treated based on the coupled mode theory. In the system sizes of the cores change slightly along the fiber axis and the propagation constant of the mode is a random function of propagation distance. A solution of the coupled mode equation is derived in a series form with the solution of the coupled mode equation for an ordered system as an initial term. The solution is applicable to the whole range of the correlation length. Using the solution the equations describing the average amplitude and the average power are derived. The equations include two coefficients, the mode coupling coefficient and the damping factor. Light launched into a core spreads over the system with propagation and the light power is transformed into the incoherent power. The mode coupling coefficient determines how light spreads and the damping factor determines the rate of the transformation of the light power into the incoherent power. The mean free path can be obtained from the distance dependence of the damping factor. When the correlation length tends to infinity the mean free path tends to infinity and light propagates coherently in the system. For short correlation lengths the damping factor is proportional to the correlation length. The result agrees with the result obtained using the perturbation solution [3]. For long correlation lengths the damping factor increases gradually compared with the linear dependence on the correlation length.

REFERENCES

1. Komiyama, A. and M. Hashimoto, *IEICE Trans.*, E77-C, 1808–1813, 1994.
2. Komiyama, A. and M. Tokimoto, *IEICE Trans.*, E83-C, 1849–1854, 2000.
3. Komiyama, A., *Proceedings of 2004 URSI EMT-S*, 260–262, 2004.